Quantifying doping-dependent electron-phonon scattering rates in silicon by inelastic x-ray scattering and first-principles lattice dynamics

Hiroshi Uchiyama,[1,*] Te-Huan Liu,[2] Toshiaki Ono,[3] Jun Fujise,[3] Bolin Liao,[4] Shenghong Ju,[5] Gang Chen,[6] and Junichiro Shiomi[5,†]

[1]*Japan Synchrotron Radiation Research Institute (JASRI), SPring-8, Koto, Sayo, Hyogo 679-5198, Japan*
[2]*School of Energy and Power Engineering, Huazhong University of Science and Technology, Wuhan 430074, China*
[3]*Advanced Evaluation and Technology Development Department, SUMCO Corporation, Imari, Saga 849-4256, Japan*
[4]*Department of Mechanical Engineering, University of California, Santa Barbara, California 93106, USA*
[5]*Department of Mechanical Engineering, The University of Tokyo, Bunkyo, Tokyo 113-8656, Japan*
[6]*Department of Mechanical Engineering, Massachusetts Institute of Technology, Cambridge, Massachusetts 02139, USA*

(Received 13 May 2023; revised 25 August 2023; accepted 25 September 2023; published 13 October 2023)

A quantitative understanding of the electron-phonon interaction is important, particularly for the thermal management of electronic devices, which are built mostly on doped silicon. Here, we performed inelastic x-ray scattering measurements on electron-doped and hole-doped bulk silicon crystals along Γ-X and directly quantified the mode- and momentum-dependent electron-phonon scattering rates of the optical phonon modes. We found the electron-phonon interaction as has been indicated; in electron-doped silicon, phonon scattering by this interaction occurs around 0.3 Γ-X for the longitudinal phonon mode, supporting the g-type intervalley scattering. In hole-doped silicon, a nonzero scattering rate is observed only in the vicinity of the zone center. The experimental results quantitatively agree with the calculations, which also explain the experimental results of the thermal conductivity.

DOI: 10.1103/PhysRevMaterials.7.104601

I. INTRODUCTION

Silicon is the imperative material for versatile applications such as diodes and transistors. The effects of doping on the transport of charge carriers, either holes or electrons, have been extensively studied. In contrast, phonon-related properties, which contribute to the thermal properties and carrier mobility, remain to be elucidated. Particularly, the electron-phonon interaction is important as it inhibits the carrier mobility and causes Joule heating. In terms of the thermal management of electronic devices, the phonon scattering by this interaction not only generates Joule heat via hot-carrier relaxation but also influences the dissipation of the heat by inhibiting the phonon transport that takes the heat out. During device operation with an electric field applied, the electrons and phonons are distributed spatiotemporally with highly nonequilibrium populations over different modes (momentum and branch). Thus knowledge of the electron-phonon scattering rates needs to be acquired in a mode-dependent fashion.

Discussions of the microscopic mechanism of the electron-phonon interaction in the optical phonon modes of doped silicon so far have relied on theoretical analyses [1,2]. The interaction induces both electron and phonon scattering. For electron-doped silicon, where the Fermi energy locates around the bottom of the conduction band at $\mathbf{k} = (k, 0, 0)$, $k \sim 0.83$, the electron-phonon scattering occurs via intervalley scattering; one is g-type scattering, where the electron is scattered from $(k, 0, 0)$ to $(-k, 0, 0)$ and the other is f-type scattering from $(k, 0, 0)$ to $(0, \pm k, 0)$ or $(0, 0, \pm k)$. In g-type scattering, the electron scattering accompanies the phonon scattering of $\mathbf{q} = (2 - 2k, 0, 0) \simeq (0.34, 0, 0)$ due to the umklapp scattering. On the other hand, for hole-doped silicon, where the Fermi energy locates around the top of the valence band, both the electron and phonon scattering are restricted around the zone center, known as intravalley scattering. Recently, owing to the expansion of computational capability, it has become accessible to perform calculations using the density-functional theory (DFT) to help understand the detailed mechanism of the electron-phonon interaction [3–10]. The calculations can explain how carrier mobility varies with the dopant, carrier concentration, and temperature [5–9]. These calculations have also established a detailed understanding of the thermal conductivity and suggest that the electron-phonon interaction can significantly enhance the phonon scattering in heavily doped silicon [3].

Experimental evidence of the electron-phonon interaction on phonon scattering is reported for acoustic phonons at a specific frequency (∼250 GHz) [11]. Inelastic neutron scattering (INS) measurements observed the renormalization of the acoustic phonon modes in doped silicon [12]. Raman scattering spectroscopy, a conventional method to study phonons with terahertz frequency, is not adequate for estimating this interaction, owing to another resonant (Fano-type) interaction with continuum electronic states [13]. To evade this resonant interaction, the observation of coherent phonons is required, and Ref. [14] succeeds in estimating the lifetime of heavily hole-doped silicon at the zone center. When we

*Corresponding author: uchiyama@spring8.or.jp
†Corresponding author: shiomi@photon.t.u-tokyo.ac.jp

broaden our perspective to other materials, INS and inelastic x-ray scattering (IXS) measurements have facilitated a comprehensive estimation of the mode-dependent phonon lifetime and renormalization [10,15–21], including the estimation of the electron-phonon interaction [10,21]. In this paper, we have conducted IXS measurements to directly probe the phonon lifetimes of the optical phonon modes along Γ-X and quantify the mode-dependent electron-phonon scattering rates. The experimental results are quantitatively reproduced by first-principles calculations. Furthermore, the calculations only including the phonon-phonon and electron-phonon interactions also reproduce the observed thermal conductivity, suggesting the impurity and/or defect scattering does not play a significant role in the phonon scattering below $\sim 10^{20}$ cm^{-3}, in contrast with electron scattering by phonons in the carrier mobility.

II. METHODS

A. Sample preparation

The doped silicon crystals were grown in SUMCO Corporation with the Czochralski (CZ) method. The doping is controlled by intentionally adding boron (for hole doping) or phosphor (for electron) during the growth. These dopants are incorporated into silicon, following the segregation coefficients of these atoms. All grown crystals contain no dislocation, confirmed by an x-ray topography method [see also Sec. 1 in the Supplemental Material (SM) [22]], while they include oxygen as an impurity (1×10^{18} cm^{-3}). The carrier concentration was evaluated from the resistivity measurements [25]; the resistivities of the lightly hole-, heavily hole-, and heavily electron-doped samples are 24.4–25.5 Ω cm (corresponding to a carrier concentration of $p^- = 5 \times 10^{14}$ cm^{-3}), 5.5 mΩ cm ($p^+ = 2 \times 10^{19}$ cm^{-3}), and $\sim$1.0 mΩ cm ($n^+ \sim 8 \times 10^{19}$ cm^{-3}), respectively. The samples utilized for this study are supposed to rarely include inactive (not ionized) dopants, because Refs. [26,27] indicate that the ratios of the inactive dopants are less than 5% for these doping levels. For the IXS measurements, the samples were cut into $20 \times 20 \times 0.8$ mm^3 size, along the (110), (1$\bar{1}$0), and (001) crystal orientations.

B. Inelastic x-ray scattering

The IXS measurements were performed on the BL35XU beamline at the SPring-8 synchrotron facility. We used the Si(11 11 11) reflection on the backscattering geometry, which corresponds to an incident x-ray energy of $h\nu = 21.747$ keV. The incident beam was focused by a bent cylindrical mirror, and the beam spot size was $\sim$70(width) $\times$ 50(height) μm^2 at the sample position. The scattered photon by the analyzers is detected by CdZnTe crystals. The total energy resolution in optics [$g(\omega)$ in Sec. 2-2 in SM [22]] varies from 1.4 to 1.8 meV [full width at half maximum (FWHM) of a Voigt function [28]], and this fluctuation depends both on the analyzers and beamline setup. Hence the energy resolution at each analyzer was estimated using the standard material, polymethyl methacrylate (PMMA), when a new beamline setup was made. Adjusting the slits before the analyzers, we obtained a momentum resolution of 0.7 nm^{-1}, or $\Delta\mathbf{Q} = (0.06, 0.06, 0.02)$ in reciprocal lattice units. All measurements were conducted at $T \sim 300$ K. Given the fact that the x-ray attenuation length of Si is relatively large (>1 mm) at this photon energy, the transmission (Laue) geometry was applied along the (001) direction. In the present study, in order to estimate the electron-phonon interaction, we focused on the optical phonons, since the phonon linewidth of the acoustic phonon is expected to be much smaller [3] than the current experimental accuracy. It is known that, in bulk silicon, the optical phonon contributes much less to the thermal conductivity than the acoustic phonon [29]. In nanostructures, however, the longitudinal optical phonon mode (LO) is expected to make a significant contribution to the thermal conductivity [29]. In order to confirm reproducibility and to obtain precise data, several measurements were conducted on two different batches. The obtained data were analyzed statistically at each momentum, $\mathbf{q} = (q00)$, along the Γ-X direction [see also Sec. 2-1 in SM [22]].

C. Calculations

We calculate the phonon scattering rates as well as the thermal conductivities considering both the phonon-phonon and phonon-electron interactions by using the QUANTUM ESPRESSO [30], SHENGBTE [31], and EPW [32] packages. A norm-conserving pseudopotential with the Perdew-Zunger exchange-correlation functional is employed in the DFT and density-functional perturbation theory (DFPT) calculations. The spin-orbit coupling is taken into account in order to capture the nondegeneracy of the valence band edge of Si. The DFT calculation is performed on Monkhorst-Pack $16 \times 16 \times 16$ k-mesh grids, and the DFPT on $6 \times 6 \times 6$ q-mesh grids. Third-order force constants are computed using a $4 \times 4 \times 4$ supercell with a cutoff distance of fourth-nearest-neighbor atoms. With these prepared inputs, the phonon-phonon scattering rates are computed on $60 \times 60 \times 60$ q-mesh grids, and the phonon-electron scattering rates are computed on $60 \times 60 \times 60$ q-mesh grids, where each grid scatters with $120 \times 120 \times 120$ k-mesh grids.

III. RESULTS AND DISCUSSION

A. Extracting phonon scattering rates

Representative raw spectra are shown in Fig. 1; the dots display IXS results of the optical phonon modes at Γ [Figs. 1(a)–1(c)] and X [Figs. 1(d)–1(i)] for the lightly hole-doped (p^-), heavily hole-doped (p^+), and heavily electron-doped (n^+) samples. In silicon, as a nonpolar semiconductor, the three optical phonon modes are degenerated at Γ, and these modes are separated to two degenerated transverse optical (TO) modes and a single LO mode at $q > 0$ in the Γ-X direction [see also Fig. S2 in SM [22]]. The spectra in Figs. 1(d)–1(f) correspond to the TO mode at X [X(TO)] and those in Figs. 1(g)–1(i) are the LO mode [X(LO)]. The green lines, or shaded areas, in Fig. 1 are the experimental resolution function [$g * h$ in Sec. 2-2 in SM [22]]. At the Γ point, the spectra for the heavily hole-doped samples show a clear broadening [p^+, the fitting result shown in black in Fig. 1(b)],

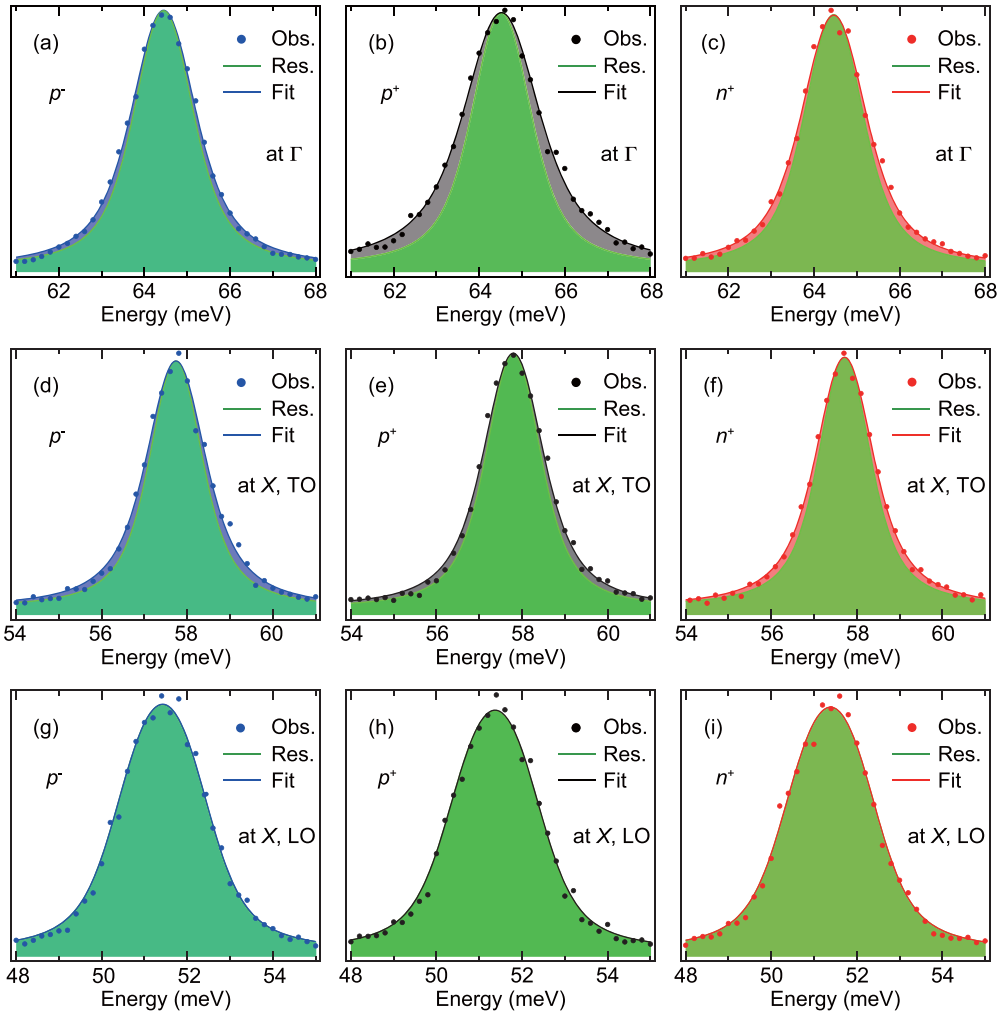

FIG. 1. Experimental phonon linewidth broadening at (a)–(c) Γ, (d)–(f) X(TO), and (g)–(i) X(LO) for lightly hole-doped (p^-), heavily hole-doped (p^+), and heavily electron-doped (n^+) samples. The green shaded areas are the experimental resolution function. The blue [(a), (d), (g) for p^-], black [(b), (e), (h) for p^+], and red [(c), (f), (i) for n^+] are the results of the fit [22]. The difference of those from the green areas corresponds to the linewidth broadening due to the phonon scattering.

while the spectra for lightly hole-doped [p^-, blue in Fig. 1(a)] and heavily electron-doped [n^+, red in Fig. 1(c)] samples show a small broadening. In the harmonic approximation, the IXS spectra and resolution function should have the same linewidth, because no phonon scattering occurs in this approximation. Under the simplified phonon self-energy assumption ($\Sigma_{\mathbf{q},j}$, for the jth phonon branch at a momentum $\mathbf{q}$), on the other hand, deviation from the harmonic approximation is expressed as a Lorentzian with a shift of Re $\Sigma_{\mathbf{q},j}$ and broadening of 2 Im $\Sigma_{\mathbf{q},j}$ [15,22]. The estimated phonon linewidth, or scattering rate (2 Im $\Sigma_{\Gamma,\mathrm{optical}}$) is ∼0.2 meV for the p^- and n^+ samples, and ∼0.7 meV for the p^+ samples [for the detailed procedure, see Sec. 2-2 in SM [22]]. This linewidth for the p^- samples is similar to that in a study of Raman measurements (∼0.3 meV) for mostly pristine, or undoped, silicon with $>10^3$ Ω cm [33]. We have performed a similar procedure for the spectra at X [Figs. 1(d)–1(i)]; the estimated phonon linewidth of TO [Figs. 1(d)–1(f)] (2 Im $\Sigma_{X,\mathrm{TO}}$) is commonly ∼0.2 meV, and that of LO [Figs. 1(g)–1(i)] (2 Im $\Sigma_{X,\mathrm{LO}}$) is ∼0 meV.

The phonon scattering rate can be divided into contributions from different events, according to the Matthiessen's rule [34],

$$2\,\mathrm{Im}\,\Sigma_{\mathbf{q},j} = 2\,\mathrm{Im}\,\Sigma^{(\mathrm{ph\text{-}ph})}_{\mathbf{q},j} + 2\,\mathrm{Im}\,\Sigma^{(\mathrm{el\text{-}ph})}_{\mathbf{q},j} + 2\,\mathrm{Im}\,\Sigma^{(\mathrm{imp})}_{\mathbf{q},j}. \quad (1)$$

In other words, the phonon linewidth consists of the phonon-phonon scattering (the phonon lifetime is given as $\tau^{(\mathrm{ph\text{-}ph})}_{\mathbf{q},j} = \hbar/2\,\mathrm{Im}\,\Sigma^{(\mathrm{ph\text{-}ph})}_{\mathbf{q},j}$), electron-phonon scattering ($\tau^{(\mathrm{el\text{-}ph})}_{\mathbf{q},j} = \hbar/2\,\mathrm{Im}\,\Sigma^{(\mathrm{el\text{-}ph})}_{\mathbf{q},j}$), and phonon scattering by impurities and/or defects ($\tau^{(\mathrm{imp})}_{\mathbf{q},j} = \hbar/2\,\mathrm{Im}\,\Sigma^{(\mathrm{imp})}_{\mathbf{q},j}$). When the sample is a single crystal with a large enough size with respect to the phonon mean free path, the boundary scattering is negligible. In a pristine silicon crystal, the contribution of the phonon-phonon scattering dominates, while the contributions of the electron-phonon and impurity/defect scattering need to be considered for the doped samples.

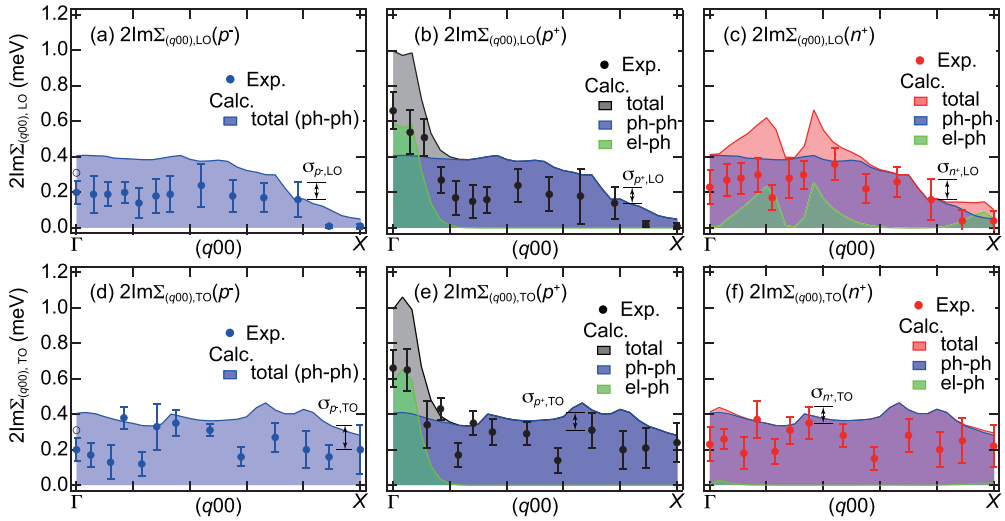

FIG. 2. Phonon scattering rates of LO and TO along Γ-X for the (a), (d) p^-, (b), (e) p^+, and (c), (f) n^+ samples. The dots are the experimentally obtained scattering rates. (a), (d) The blue shaded areas correspond to the phonon-phonon scattering rates of the p^- samples. (b), (e) The black and (c), (f) red shaded areas are the calculated phonon scattering rates of p^+ and n^+, that consist of the contributions of the phonon-phonon (blue) and electron-phonon (green) interactions. Open circles in (a) and (d) indicate the phonon scattering rate obtained from the Raman measurement [33]. The error bars are the standard deviation at each q; (a), (d) $\pm\sigma_{p^-,j}$, (b), (e) $\pm\sigma_{p^+,j}$, and (c), (f) $\pm\sigma_{n^+,j}$ (j = LO, TO).

B. Momentum-dependent scattering rates

The comparisons between the measured and calculated phonon scattering rates ($2\,\mathrm{Im}\,\Sigma_{\mathbf{q},j}$) are depicted as functions of the momentum along the Γ-X direction in Fig. 2. The measurements were achieved several times at each q, as mentioned above (the number of trials N is $N = 5$–20 [22]), and the standard deviation σ is displayed as error bars ($\pm\sigma$), as seen in Fig. 2. The phonon-phonon scattering (blue shaded areas) well supports the experimental spectra (dots) for the p^- samples [Figs. 2(a) and 2(d)]. Furthermore, for the p^+ and n^+ samples, the calculated scattering rates (black and red shaded areas), that are the sum of the contributions of the phonon-phonon (blue) and electron-phonon (green) interactions, also agree with the experimental results (dots) [Figs. 2(b), 2(c), 2(e), and 2(f)]. It is worth noting that the calculated phonon-phonon scattering rate (blue) reasonably agrees with that in a previous study [35].

From Figs. 2(a)–2(f), we can experimentally extract the contribution of the electron-phonon interaction, $2\,\mathrm{Im}\,\Sigma^{(\mathrm{el\text{-}ph})}_{\mathbf{q},j}$ (j = LO, TO), using the difference of experimentally obtained $2\,\mathrm{Im}\,\Sigma_{\mathbf{q},j}$, based on Eq. (1),

$$2\,\mathrm{Im}\,\Sigma^{(\mathrm{el\text{-}ph})}_{\mathbf{q},j}(p^+) = 2\,\mathrm{Im}\,\Sigma_{\mathbf{q},j}(p^+) - 2\,\mathrm{Im}\,\Sigma_{\mathbf{q},j}(p^-)$$

and

$$2\,\mathrm{Im}\,\Sigma^{(\mathrm{el\text{-}ph})}_{\mathbf{q},j}(n^+) = 2\,\mathrm{Im}\,\Sigma_{\mathbf{q},j}(n^+) - 2\,\mathrm{Im}\,\Sigma_{\mathbf{q},j}(p^-), \quad (2)$$

under the assumption that the phonon linewidth of the p^- samples only includes the phonon-phonon scattering [$2\,\mathrm{Im}\,\Sigma_{\mathbf{q},j}(p^-) = 2\,\mathrm{Im}\,\Sigma^{(\mathrm{ph\text{-}ph})}_{\mathbf{q},j}$]. The results are shown in Fig. 3. In this figure, the error bars are taken from the larger value of σ in Fig. 2 [i.e., $\max(\sigma_{p^+,\mathrm{LO}}, \sigma_{p^-,\mathrm{LO}})$, $\max(\sigma_{n^+,\mathrm{LO}}, \sigma_{p^-,\mathrm{LO}})$, and so on]. Note, these error bars mostly agree with the 99% highest density intervals (HDIs) from a Bayesian inference at the momenta (q00) which we are interested in [see Sec. 2-3 in SM [22] for details]. For the p^+ samples, a large scattering rate is observed only in the vicinity of Γ (for example, the experimentally estimated phonon scattering rate at Γ, $2\,\mathrm{Im}\,\Sigma^{(\mathrm{el\text{-}ph})}_{\Gamma,\mathrm{optical}}$, is 0.46 ± 0.10 meV), that agrees with the calculations quantitatively [see Figs. 3(a) and 3(b); see also Sec. 2-4 in SM [22]]. This large scattering rate corresponds to the intravalley scattering for hole-doped silicon [1,2,9].

For the n^+ samples, some weak feature is observed broadly in the range between $q \sim 0.2$ and $q \sim 0.7$ in LO [dots in Fig. 3(c)], while no clear feature is observed in TO [Fig. 3(d)]. These experimental results reasonably follow the calculations (green lines). The LO scattering centered around $q \sim 0.3$ corresponds to the g-type intervalley scattering. From the group theory, or the selection rules, this g-type phonon scattering is prohibited for TO and only allows LO [36,37], supporting both our measurements and calculations. The estimated scattering rate, $2\,\mathrm{Im}\,\Sigma^{(\mathrm{el\text{-}ph})}_{(0.33,0,0),\mathrm{LO}}$, for the n^+ samples is 0.11 ± 0.10 meV.

C. Phonon dispersion relations

Under a strong electron-phonon interaction, a peak renormalization, nonzero $\mathrm{Re}\,\Sigma_{\mathbf{q},j}$, is expected. In fact, Ref. [12] reports the renormalization of the acoustic phonon modes for $>5 \times 10^{19}$ cm^{-3} doped silicon. In the current measurements, on the other hand, all the measured phonon dispersion relations [dots in Figs. 4(a) and 4(b)] agree with the calculated dispersion in the harmonic approximation (blue lines) within the experimental uncertainty, and no clear renormalization is observed.

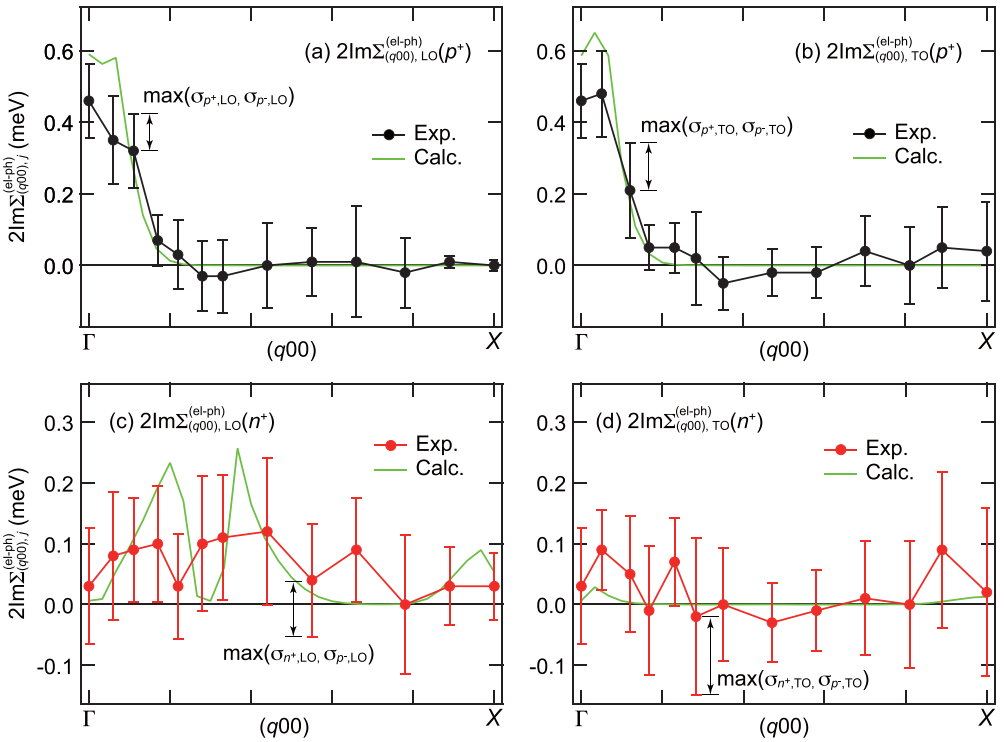

FIG. 3. (a), (b) Experimentally obtained (dots) and calculated (lines) electron-phonon scattering rates of (a) LO and (b) TO for the p^+ samples. The error bars indicate max($\sigma_{\mathrm{p}^+,j}$, $\sigma_{\mathrm{p}^-,j}$) (j = LO, TO). (c), (d) The electron-phonon scattering rates of (c) LO and (d) TO for the n^+ samples. The error bars indicate max($\sigma_{\mathrm{n}^+,j}$, $\sigma_{\mathrm{p}^-,j}$).

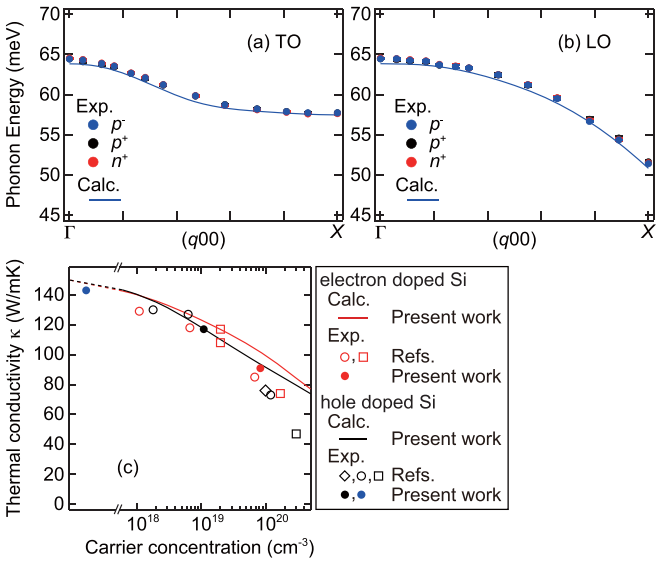

FIG. 4. (a), (b) Optical phonon dispersion relations along Γ-X. The dots are the experimentally obtained phonon dispersion relations of (a) LO and (b) TO for the p^-, p^+, and n^+ samples. The lines are the calculated dispersion in the harmonic approximation, without including any phonon scattering. Each dot includes the standard deviation σ as an error bar of $\pm\sigma$, while it is not clearly visible in this figure. (c) The carrier concentration dependence of the thermal conductivity. The experimentally obtained results are taken from Refs. [38] (◇), [39] (○), and [40] (□), in addition to the present study (solid circles). The red and black lines are the calculated thermal conductivity.

D. Thermal conductivity

In the case of electron scattering, the ionized impurity scattering strongly suppresses the mobility at $\gtrsim 10^{16}$ cm^{-3} [9]. In the case of phonon scattering, on the other hand, the impurity/defect scattering seems to make a small contribution, because the experimentally observed phonon scattering rates are well reproduced by the calculations which consist of phonon-phonon and electron-phonon scattering only [Figs. 2(b), 2(c), 2(e), and 2(f)]. To confirm this, we have measured the thermal conductivity at T = 296–297 K [for the detailed method, see Sec. 3 in SM [22]], and summarized the measured and calculated thermal conductivity in Fig. 4(c). In Fig. 4(c), the experimentally reported values for single crystals in previous studies [38–40] are also displayed. In the current calculations, the (lattice) thermal conductivity κ can be written as

$$\kappa = \frac{1}{3}\sum_{\mathbf{q},j} C_{\mathbf{q},j} v^2_{\mathbf{q},j} \tau_{\mathbf{q},j}. \tag{3}$$

Here, $v_{\mathbf{q},j}$ is the phonon group velocity and $C_{\mathbf{q},j}$ is the specific heat. The calculations only including the phonon-phonon scattering $\tau^{(\mathrm{ph\text{-}ph})}_{\mathbf{q},j}$ and the electron-phonon scattering $\tau^{(\mathrm{el\text{-}ph})}_{\mathbf{q},j}$ [lines in Fig. 4(c)] well reproduce the experimental values, except for the higher concentration ($>10^{20}$ cm^{-3}). This indicates that the influence of the impurity/defect scattering is minute in the current study, probably because the electrons and phonons have different mean free paths [5].

IV. CONCLUSIONS

In summary, our work demonstrates a direct experimental extraction of momentum-dependent electron-phonon scattering rates in the optical phonon mode of heavily doped silicon. While the optical phonon dispersion relations are reproduced by a harmonic approximation and do not depend on the type of the doping, their scattering rates significantly differ. The extracted electron-phonon scattering rates agree well with those obtained from the first-principles lattice dynamics. Furthermore, both the measurements and calculations indicate that, for the samples investigated ($\lesssim 10^{20}$ cm^{-3} at $T \sim 300$ K), the phonon-phonon and electron-phonon scattering dominates the phonon scattering. Since the electron-phonon interaction commonly exists in semiconducting materials, the direct estimation in this study can be applied to other materials.

ACKNOWLEDGMENTS

IXS measurements at SPring-8 were performed under Proposals No. 2016A1324, No. 2016B1947, No. 2017B1340, No. 2017B1966, No. 2018A1486, No. 2018B1530, No. 2018B2020, and No. 2019A2026. B.L. acknowledges support by the U.S. National Science Foundation under Award No. CBET-1846927.

[1] M. Lundstrom, *Fundamentals of Carrier Transport* (Cambridge University Press, Cambridge, UK, 2000).

[2] P. Yu and M. Cardona, *Fundamentals of Semiconductors: Physics and Materials Properties* (Springer, Berlin, 2010).

[3] B. Liao, B. Qiu, J. Zhou, S. Huberman, K. Esfarjani, and G. Chen, Significant reduction of lattice thermal conductivity by the electron-phonon interaction in silicon with high carrier concentrations: A first-principles study, Phys. Rev. Lett. **114**, 115901 (2015).

[4] T.-H. Liu, J. Zhou, M. Li, Z. Ding, Q. Song, B. Liao, L. Fu, and G. Chen, Electron mean-free-path filtering in Dirac material for improved thermoelectric performance, Proc. Natl. Acad. Sci. USA **115**, 879 (2018).

[5] B. Qiu, Z. Tian, A. Vallabhaneni, B. Liao, J. M. Mendoza, O. D. Restrepo, X. Ruan, and G. Chen, First-principles simulation of electron mean-free-path spectra and thermoelectric properties in silicon, Europhys. Lett. **109**, 57006 (2015).

[6] J. Ma, A. S. Nissimagoudar, and W. Li, First-principles study of electron and hole mobilities of Si and GaAs, Phys. Rev. B **97**, 045201 (2018).

[7] S. Poncé, E. R. Margine, and F. Giustino, Towards predictive many-body calculations of phonon-limited carrier mobilities in semiconductors, Phys. Rev. B **97**, 121201(R) (2018).

[8] S. Poncé, F. Macheda, E. R. Margine, N. Marzari, N. Bonini, and F. Giustino, First-principles predictions of Hall and drift mobilities in semiconductors, Phys. Rev. Res. **3**, 043022 (2021).

[9] Z. Li, P. Graziosi, and N. Neophytou, Deformation potential extraction and computationally efficient mobility calculations in silicon from first principles, Phys. Rev. B **104**, 195201 (2021).

[10] F. Caruso, M. Hoesch, P. Achatz, J. Serrano, M. Krisch, E. Bustarret, and F. Giustino, Nonadiabatic Kohn anomaly in heavily boron-doped diamond, Phys. Rev. Lett. **119**, 017001 (2017).

[11] J. Zhou, H. D. Shin, K. Chen, B. Song, R. A. Duncan, Q. Xu, A. A. Maznev, K. A. Nelson, and G. Chen, Direct observation of large electron-phonon interaction effect on phonon heat transport, Nat. Commun. **11**, 6040 (2020).

[12] L. Pintschovius, J. A. Vergés, and M. Cardona, Self-energies of phonons in heavily doped *n*- and *p*-type silicon, Phys. Rev. B **26**, 5658 (1982).

[13] F. Cerdeira, T. A. Fjeldly, and M. Cardona, Effect of free carriers on zone-center vibrational modes in heavily doped *p*-type Si. II. Optical modes, Phys. Rev. B **8**, 4734 (1973).

[14] K. Kato, K. Oguri, H. Sanada, T. Tawara, T. Sogawa, and H. Gotoh, Determination of phonon decay rate in *p*-type silicon under Fano resonance by measurement of coherent phonons, AIP Adv. **5**, 097152 (2015).

[15] H. Uchiyama, Y. Oshima, R. Patterson, S. Iwamoto, J. Shiomi, and K. Shimamura, Phonon lifetime observation in epitaxial ScN film with inelastic x-ray scattering spectroscopy, Phys. Rev. Lett. **120**, 235901 (2018).

[16] O. Delaire, J. Ma, K. Marty, A. F. May, M. A. McGuire, M.-H. Du, D. J. Singh, A. Podlesnyak, G. Ehlers, M. D. Lumsden, and B. C. Sales, Giant anharmonic phonon scattering in PbTe, Nat. Mater. **10**, 614 (2011).

[17] J. W. L. Pang, W. J. L. Buyers, A. Chernatynskiy, M. D. Lumsden, B. C. Larson, and S. R. Phillpot, Phonon lifetime investigation of anharmonicity and thermal conductivity of UO_2 by neutron scattering and theory, Phys. Rev. Lett. **110**, 157401 (2013).

[18] J. Ma, O. Delaire, A. F. May, C. E. Carlton, M. A. McGuire, L. H. VanBebber, D. L. Abernathy, G. Ehlers, T. Hong, A. Huq, W. Tian, V. M. Keppens, Y. Shao-Horn, and B. C. Sales, Glass-like phonon scattering from a spontaneous nanostructure in $AgSbTe_2$, Nat. Nanotechnol. **8**, 445 (2013).

[19] D. J. Voneshen, K. Refson, E. Borissenko, M. Krisch, A. M. Hoesch, M. Roger, L. Gannon, A. T. Boothroyd, S. Uthayakumar, D. G. Porter, and J. P. Goff, Suppression of thermal conductivity by rattling modes in thermoelectric sodium cobaltate, Nat. Mater. **12**, 1028 (2013).

[20] P.-F. Lory, S. Pailhès, V. M. Giordano, H. Euchner, H. D. Nguyen, R. Ramlau, H. Borrmann, M. Schmidt, M. Baitinger, M. Ikeda, P. Tomeš, M. Mihalkovič, C. Allio, M. R. Johnson, H. Schober, Y. Sidis, F. Bourdarot, L. P. Regnault, J. Ollivier, S. Paschen *et al.*, Direct measurement of individual phonon lifetimes in the clathrate compound $Ba_{7.81}Ge_{40.67}Au_{5.33}$, Nat. Commun. **8**, 491 (2017).

[21] M. P. Jiang, M. Trigo, I. Savić, S. Fahy, É. D Murray, C. Bray, J. Clark, T. Henighan, M. Kozina, M. Chollet, J. M. Glownia, M. C. Hoffmann, D. Zhu, O. Delaire, A. F. May, B. C. Sales, A. M. Lindenberg, P. Zalden, T. Sato, R. Merlin, and D. A. Reis, The origin of incipient ferroelectricity in lead telluride, Nat. Commun. **7**, 12291 (2016).

[22] See Supplemental Material at http://link.aps.org/supplemental/10.1103/PhysRevMaterials.7.104601 for a typical result of the x-ray topography measurements, the detailed procedures in

analyzing the IXS results, and the procedure of the thermal conductivity measurements, which includes Refs. [23,24].

[23] A. A. Maradudin and A. E. Fein, Scattering of neutrons by an anharmonic crystal, Phys. Rev. **128**, 2589 (1962).

[24] J. Salvatier, T. Wiecki, and C. Fonnesbeck, Probabilistic programming in Python using PyMC3, PeerJ Comput. Sci. **2**, e55 (2016).

[25] W. R. Thurber, R. L. Mattis, Y. M. Liu, and J. J. Filliben, *The Relationship between Resistivity and Dopant Density for Phosphorus- and Boron-Doped Silicon*, NBS Special Publication No. 400-64 (National Bureau of Standards, Washington, DC, 1981).

[26] P. P. Altermatt, A. Schenk, and G. Heiser, A simulation model for the density of states and for incomplete ionization in crystalline silicon. I. Establishing the model in Si:P, J. Appl. Phys. **100**, 113714 (2006).

[27] P. P. Altermatt, A. Schenk, B. Schmithusen, and G. Heiser, A simulation model for the density of states and for incomplete ionization in crystalline silicon. II. Investigation of Si:As and Si:B and usage in device simulation, J. Appl. Phys. **100**, 113715 (2006).

[28] J. J. Olivero and R. L. Longbothum, Empirical fits to the Voigt line width: A brief review, J. Quant. Spectrosc. Radiat. Transfer **17**, 233 (1977).

[29] Z. Tian, K. Esfarjani, J. Shiomi, A. S. Henry, and G. Chen, On the importance of optical phonons to thermal conductivity in nanostructures, Appl. Phys. Lett. **99**, 053122 (2011).

[30] P. Giannozzi, S. Baroni, N. Bonini, M. Calandra, R. Car, C. Cavazzoni, D. Ceresoli, G. L. Chiarotti, M. Cococcioni, I. Dabo, A. Dal Corso, S. de Gironcoli, S. Fabris, G. Fratesi, R. Gebauer, U. Gerstmann, C. Gougoussis, A. Kokalj, M. Lazzeri, L. Martin-Samos, N. Marzari *et al.*, QUANTUM ESPRESSO: A modular and open-source software project for quantum simulations of materials, J. Phys.: Condens. Matter **21**, 395502 (2009).

[31] W. Li, J. Carrete, N. A. Katcho, and N. Mingo, ShengBTE: A solver of the Boltzmann transport equation for phonons, Comput. Phys. Commun. **185**, 1747 (2014).

[32] S. Poncé, E. R. Margine, C. Verdi, and F. Giustino, EPW: Electron-phonon coupling, transport and superconducting properties using maximally localized Wannier functions, Comput. Phys. Commun. **209**, 116 (2016).

[33] J. Ménendez and M. Cardona, Temperature dependence of the first-order Raman scattering by phonons in Si, Ge, and α-Sn: Anharmonic effects, Phys. Rev. B **29**, 2051 (1984).

[34] J. Ziman, *Electrons and Phonons* (Oxford University Press, Oxford, UK, 1960).

[35] G. Deinzer, G. Birner, and D. Strauch, *Ab initio* calculation of the linewidth of various phonon modes in germanium and silicon, Phys. Rev. B **67**, 144304 (2003).

[36] H. W. Streitwolf, Intervalley scattering selection rules for Si and Ge, Phys. Status Solidi B **37**, K47 (1970).

[37] M. Lax and J. L. Birman, Intervalley scattering selection rules for Si and Ge, Phys. Status Solidi B **49**, K153 (1972).

[38] M. Asheghi, K. Kurabayashi, R. Kasnavi, and K. E. Goodson, Thermal conduction in doped single-crystal silicon films, J. Appl. Phys. **91**, 5079 (2002).

[39] Y. Ohishi, J. Xie, Y. Miyazaki, Y. Aikebaier, H. Muta, K. Kurosaki, S. Yamanaka, N. Uchida, and T. Tada, Thermoelectric properties of heavily boron- and phosphorus-doped silicon, Jpn. J. Appl. Phys. **54**, 071301 (2015).

[40] G. A. Slack, Thermal conductivity of pure and impure silicon, silicon carbide, and diamond, J. Appl. Phys. **35**, 3460 (1964).